

Tailoring Nonstoichiometry and Mixed Ionic Electronic Conductivity in $\text{Pr}_{0.1}\text{Ce}_{0.9}\text{O}_{2-\delta}/\text{SrTiO}_3$ Heterostructures

George F. Harrington,^{*,†,‡,§,||,§} Dmitri Kalaev,^{||} Bilge Yildiz,^{⊥,||} Kazunari Sasaki,^{†,‡} Nicola H. Perry,^{#,§} and Harry L. Tuller^{||,§}

[†]Center of Coevolutionary Research for Sustainable Communities (C²RSC), [‡]Next-Generation Fuel Cell Research Centre, and

[§]International Institute for Carbon-Neutral Energy Research (I²CNER), Kyushu University, 744 Motooka, Nishi-ku, Fukuoka 819-0395, Japan

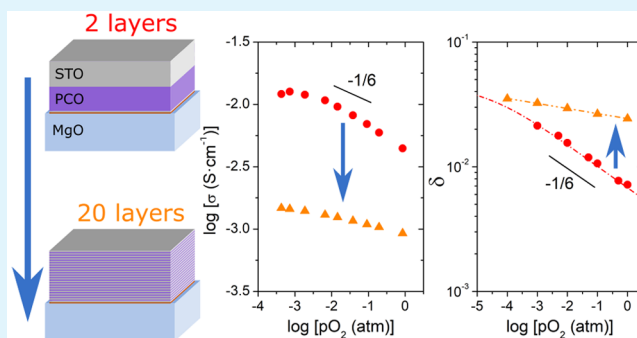
^{||}Department of Materials Science and Engineering and [⊥]Department of Nuclear Science and Engineering, Massachusetts Institute of Technology, 77 Massachusetts Avenue, Cambridge, Massachusetts 02139, United States

[#]Department of Materials Science and Engineering and Materials Research Laboratory, University of Illinois at Urbana-Champaign, Urbana, Illinois 61801, United States

Supporting Information

ABSTRACT: The oxygen deficiency or excess, as reflected in the nonstoichiometry of oxide films, plays a crucial role in their functional properties for applications such as micro solid oxide fuel cells, catalysis, sensors, ferroelectrics, and memristors. High concentrations of oxygen vacancies may be beneficial or detrimental according to the application, and hence there is interest in controlling the oxygen content of films without resorting to compositional changes. Here, we demonstrate that substantial changes in the nonstoichiometry of $\text{Pr}_{0.1}\text{Ce}_{0.9}\text{O}_{2-\delta}$ (PCO), a model mixed ionic electronic conductor, can be achieved by fabricating multilayers with an inert material, SrTiO_3 (STO). We fabricated heterostructures using pulsed laser deposition, keeping the total thickness of PCO and STO constant while varying the number of layers and thickness of each individual layer, to probe the effects of the PCO/STO interfaces. Conductivity measurements as a function of oxygen partial pressure (P_{O_2}) and temperature showed a significant weakening of the P_{O_2} dependence compared to bulk PCO, which scaled with the density of interfaces. We confirmed that this change was due to variations in nonstoichiometry, by optical transmission measurements, and show that the lower oxygen content is consistent with a decrease in the effective oxygen reduction enthalpy of PCO. These results exemplify the dramatic differences in properties between films and their bulk counterparts, achievable by interface engineering, and provide generalized insight into tailoring the properties of mixed ionic electronic conductors at the nanoscale.

KEYWORDS: mixed ionic electronic conductors, oxide heterointerfaces, electro-chemo-mechanics, multilayer heterostructures, ceria



1. INTRODUCTION

In crystalline oxide materials, the concentration of oxygen vacancies, or degree of nonstoichiometry, plays a crucial role in the capability of the material to transport oxygen. The ability of certain oxides to conduct either oxygen ions or both oxygen ions and electrons/holes at a significant rate forms the basis for a range of electrochemical devices such as solid oxide fuel cells (SOFCs), solid oxide electrolyzer cells, gas permeation membranes, sensors, and next-generation information storage.^{1–6} For other applications such as ferroelectrics and piezoelectrics, oxygen vacancies are detrimental,^{7,8} so there is great interest in tailoring their concentration and mobility.

Changes in oxygen deficiency also result in dilation of the crystalline lattice, known as chemical expansion, and hence, there is a coupling between the chemical, electrical, and mechanical properties of nonstoichiometric oxides, referred to

as electro-chemo-mechanics.⁹ As such, confined systems such as thin films are being investigated as a route to improved functional properties, shifting the paradigm of materials development away from compositional tuning and searching for new functional oxides. Thin-film nonstoichiometric oxides also have direct applications in the form of micro-SOFCs, memristors, photovoltaics, sensors, and various electronic circuit components.^{10–13}

At heterogeneous interfaces between two dissimilar oxides, there are several effects that can locally modify the properties of the material compared to the bulk, which stem from electro-chemo-mechanical coupling. At the interface plane, materials

Received: May 22, 2019

Accepted: August 21, 2019

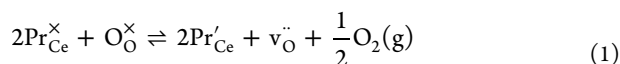
Published: August 21, 2019

can be mechanically constrained such that chemical expansion or relaxation due to changes in the nonstoichiometry can no longer occur freely along the interface plane, which could result in anisotropic mechanical properties or changes in the equilibrium oxygen deficiency for a given environment (temperature, oxygen partial pressure (P_{O_2})). Further, induced strain due to an epitaxial lattice mismatch or stresses occurring in films during growth have been investigated as a method for modifying the migration barrier for oxygen vacancy hopping, whereby a tensile strain decreases the migration energy and enhances diffusivity, and a compressive strain increases the migration barrier and diminishes diffusivity.^{14–16}

At the structural cores of both heterogeneous and homogeneous interfaces (grain boundaries), an excess of charged species can accumulate, resulting in the formation of space charge layers. Typically, the space charge profile is approximated by the Gouy–Chapman or Mott–Schottky models, and the width of the space charge layer is on the order of the Debye length, which is often less than 1 nm in functional oxides with a high concentration of charged defects. These models are only truly valid at low defect concentrations, and experimental evidence suggests that the space charge regions in materials with a high substituent concentration extend to larger distances. Mebane and De Souza recently proposed a model explaining this discrepancy by introducing gradient energy terms in a combined Poisson–Boltzmann and Cahn–Hilliard model.¹⁷ Vikrant et al. suggested that the same behavior can be explained by including mechanical effects experienced at interfaces due to the changes in composition compared to the bulk.¹⁸

Therefore, it is valuable to understand how electrical, chemical, and mechanical properties change when a high density of interfaces is introduced into a solid. Praseodymium-substituted ceria ($\text{Pr}_x\text{Ce}_{1-x}\text{O}_{2-\delta}$, PCO) is an excellent model mixed ionic electronic conductor to study such effects. PCO has a cubic fluorite structure, with a wide stability range in terms of temperature, P_{O_2} , or Pr content of which it can accommodate high concentrations.¹⁹ Furthermore, PCO undergoes large changes in the lattice parameters with changes in oxygen nonstoichiometry.²⁰ PCO has been extensively studied in polycrystalline form, and the conductivity is well described as a function of oxygen partial pressure^{19,21} and can be correlated to the nonstoichiometry from thermogravimetric analysis and chemical expansion behavior from dilatometry and in situ X-ray diffraction measurements.^{20,22}

At relatively high P_{O_2} ($>10^{-10}$ atm), oxygen vacancy formation is described by eq 1 in Kröger–Vink notation



where $\text{Pr}_{\text{Ce}}^{\times}$ and Pr_{Ce}' are Pr^{4+} and Pr^{3+} on cerium sites, respectively, $\text{O}_{\text{O}}^{\times}$ is an oxygen ion on an oxygen site, and $\text{v}_{\text{O}}^{\bullet\bullet}$ is a vacant oxygen site with a relative positive charge of two. This reaction takes place according to the mass action relationship given in eq 2.

$$\frac{[\text{Pr}_{\text{Ce}}']^2 [\text{v}_{\text{O}}^{\bullet\bullet}] P_{O_2}^{1/2}}{[\text{Pr}_{\text{Ce}}^{\times}]^2 [\text{O}_{\text{O}}^{\times}]} = k_{r,\text{Pr}}^0 \exp\left(-\frac{\Delta H_{r,\text{Pr}}}{k_B T}\right) \quad (2)$$

$\Delta H_{r,\text{Pr}}$ is the enthalpy of reduction, $k_{r,\text{Pr}}^0$ is a preexponential term, and P_{O_2} is the oxygen partial pressure, T is the temperature, and k_B is the Boltzmann constant. Within this

P_{O_2} range, charge neutrality is preserved via the following relationship.

$$[\text{Pr}_{\text{Ce}}'] = 2[\text{v}_{\text{O}}^{\bullet\bullet}] \quad (3)$$

Also, the mass and site conservation is preserved according to

$$[\text{Pr}_{\text{Ce}}'] + [\text{Pr}_{\text{Ce}}^{\times}] = [\text{Pr}_{\text{Ce}}]_{\text{total}} = 0.1[\text{Pr}_{0.1}\text{Ce}_{0.9}\text{O}_{2-\delta}] \quad (4)$$

As the P_{O_2} decreases from atmospheric pressure, the vacancy concentration increases facilitated by the reduction of Pr^{4+} to Pr^{3+} , leading to ionic conductivity in the form of oxygen vacancy hopping on the anion sublattice. Simultaneously, the multivalent Pr on the cation sublattice enables electronic conductivity in the form of small polaron hopping, leading to mixed ionic electronic behavior. As the P_{O_2} decreases further, the Pr^{3+} concentration will saturate such that all the Pr can be assumed to be in the reduced state ($3+$), polaron hopping will be suppressed, and PCO will behave as a pure ionic conductor.

Another property of PCO, which makes it such an excellent model system for study, is that the redox state can be monitored optically.²³ The Pr substituent forms an impurity band in the CeO_2 optical band gap, which may facilitate optical transitions depending on the valance of Pr.²³ At higher P_{O_2} , when Pr is largely in the $4+$ state, the impurity band induces a broad absorption in the visible spectrum resulting in a red/orange coloration. As the P_{O_2} decreases and the Pr^{4+} is reduced to Pr^{3+} , electrons are localized on the Pr acceptor levels, and the impurity band becomes fully occupied, resulting in a change from red/orange to transparent. The absorption of light by PCO follows the Beer–Lambert law,²⁴ as described by

$$I_T = I_0 \exp(-\alpha w) \quad (5)$$

where I_T and I_0 are the transmitted and incident light intensities, respectively, w is the path length of the light beam through the solid, and α is the optical absorption coefficient. The optical absorption coefficient due to Pr^{4+} can be related to the concentration by a molar extinction coefficient, $\epsilon_{\text{Pr}^{4+}}$, as follows:

$$\alpha_{\text{Pr}^{4+}} = \epsilon_{\text{Pr}^{4+}} [\text{Pr}^{4+}] \quad (6)$$

The oxygen nonstoichiometry of PCO films has been studied extensively. Primarily, this has been in the form of PCO films grown on yttria-stabilized zirconia (YSZ) substrates and investigated both electrically through chemical capacitance measurements,^{25–27} as well as optically.^{24,28,29} Consistently, the oxygen substoichiometry of PCO is found to be higher (i.e., oxygen vacancy concentrations are higher), and the enthalpy of reduction, $H_{r,\text{Pr}}$, is found to be lower for films than for bulk polycrystalline ceramics. This has also been confirmed through a piezoelectric resonant microbalance study.³⁰ Films have also been reported to demonstrate changes in chemical expansion compared to bulk samples according to in situ XRD,³¹ and wafer curvature measurements,³² and reduced Young's elastic modulus, as measured by nanoindentation,³³ which has been attributed to differences in oxygen vacancy concentration.³⁴

There are several key differences between bulk ceramics and films: (1) the large volume fraction of the film/substrate interface, (2) the large volume fraction of the surface (film/gas interface), and (3) the possibility of substantially higher density of extended defects such as grain boundaries and threading dislocations. Each of these features may facilitate

mechanical constraint, induced lattice strain or relaxation, and space charge layers, such that any one or combination of these features could be the cause of the discrepancies observed between films and ceramics.

Recently, using transmission electron microscopy (TEM) and electron energy loss spectroscopy (EELS), Swallow et al. demonstrated that the substrate/film interface does indeed modify the properties of PCO films.³⁵ The authors observed that chemical expansion was anisotropic, such that the strain in the interface plane was less pronounced than the strain perpendicular to the interface. Furthermore, it was shown that the lattice expansion (and anisotropy) varied as a function of the distance from the interface. The surface of PCO films have also recently been shown to have varying properties from bulk behavior by Lu et al., utilizing in operando X-ray photoelectron spectroscopy.³⁶ A substantially higher concentration of Pr^{3+} was found on the surface in comparison to that expected for the bulk, combined with a weaker P_{O_2} dependence.

It has also been demonstrated that grain boundaries vary the properties of PCO films. Sheth et al. employed wafer curvature measurements to observe an increase in the stress of PCO films as the density of grain boundaries increased, indicating an increase in the chemical expansion at the grain boundaries.³⁷ The authors proposed that space charge regions with an excess of Pr^{3+} and a deficiency of oxygen vacancies could explain their findings. An enrichment of Gd and Pr cations at the grain boundaries of Gd/Pr-substituted CeO_2 has been reported by TEM and EELS measurements.³⁸ An increase in the reduced Ce^{3+} concentration was also observed over similar regions, which the author suggested indicates an accumulation of oxygen vacancies.

In this study, we investigate the effects of confinement on the defect properties of PCO by fabricating heterostructures of PCO with SrTiO_3 (STO). STO is a relatively inert material within the temperature and P_{O_2} range investigated in which it has a much lower conductivity (see Figure S10) and low optical absorbance for visible light³⁹ and undergoes minimal chemical expansion⁴⁰ compared with PCO. By varying numbers of layers and layer thickness in the heterostructures, we keep the total volume of PCO constant while systematically changing the interface density. By measuring the electrical conductivity and optical absorption of the multilayers, we demonstrate changes in the transport properties and defect concentrations, which can be tailored as a function of interface density. PCO is an ideal model mixed ionic electronic conductor to study changes in conductivity and non-stoichiometry in oxide films, and hence, the findings reported here should be informative for developing electroceramics for a wide range of applications.

2. METHODS

2.1. Multilayer Sample Fabrication. Thin-film heterostructures of $\text{Pr}_{0.1}\text{Ce}_{0.9}\text{O}_{2-\delta}$ (PCO) and SrTiO_3 (STO) were deposited by pulsed laser deposition (PLD, AOV Co Ltd., Japan) on 10×10 mm (001) MgO substrates (CrysTec GmbH, Germany) after a double buffer layer of BaZrO_3 (BZO) and STO was deposited. The PCO target was fabricated from nitrate precursors $\text{Pr}(\text{NO}_3)_3 \cdot 6\text{H}_2\text{O}$ (99.9%, Mitsuwa, Japan) and $\text{Ce}(\text{NO}_3)_3 \cdot 6\text{H}_2\text{O}$ (99.99%, Sigma-Aldrich Co., USA), as reported in ref 41. The STO (99.9%, Wako Pure Chemical Industries, Ltd., Japan) and BZO (98%, Sigma-Aldrich Co., USA) were prepared from commercial powders, uniaxially pressed at ~ 25 MPa into cylindrical pellets, and sintered for 10 h at 1500 and 1650

$^{\circ}\text{C}$, respectively. Phase purity was confirmed for all samples using X-ray diffraction.

The multilayered films were deposited using a 248 nm KrF excimer laser (Lambda Physik COMPex 102) operating at 2 Hz. The laser energy was set to 250 mJ, measured as 155 mJ directly outside the chamber, and focused to an area of about 5 mm^2 yielding a fluence of approximately 3.1 J cm^{-2} . The substrates were heated from behind using an IR lamp set to 750°C by the manufacture's calibration. Prior to deposition, approximately 200 nm-thick films of Pt was sputtered (TS-DC.RF303, Pascal Corp., Japan) onto the backside of the MgO substrates, to allow for effective absorption of the IR radiation and subsequent heating of the substrates. During deposition, the oxygen pressure was maintained at 2.5 Pa, and the substrate and target were continuously rotated. The growth rate of each material was calibrated using X-ray reflectivity (XRR) and found to be 0.078 nm/pulse for PCO, 0.076 nm/pulse for STO, and 0.070 nm/pulse for BZO.

For each sample, 5 nm of BZO was deposited, followed by 5 nm of STO and then the PCO/STO heterostructure. The double buffer layer of BZO and STO facilitates the epitaxial growth of fluorite-structured CeO_2 on rock salt-structured MgO, while ensuring that the electrical conductance of the substrate platform is negligible compared to the multilayers.⁴² The number of PCO and STO layers, and thickness of each layer, were varied while keeping the total thickness of the PCO and STO constant at 100 nm each. Table 1

Table 1. Multilayer Structures with the Structure $\text{MgO}/\text{BZO}(5 \text{ nm})/\text{STO}(5 \text{ nm})/(\text{PCO}(d \text{ nm}) + \text{STO}(d \text{ nm})) \times n$

sample designation	number of bilayers (n)	thickness of layers (d) (nm)
$(100 + 100) \times 1$	1	100
$(50 + 50) \times 2$	2	50
$(20 + 20) \times 5$	5	20
$(10 + 10) \times 10$	10	10
$(5 + 5) \times 20$	20	5

shows the sample design used in this study and the nomenclature used. After deposition, the samples were cooled in an oxygen pressure of 200 Pa over approximately 2 h and then subsequently annealed in a tubular furnace at 700°C for 2 h in synthetic air with a $5^{\circ}\text{C min}^{-1}$ heating/cooling rate.

2.2. Structural Characterization. X-ray diffraction (XRD) was used to assess the orientation, crystalline quality, and lattice parameters of the multilayers, using a diffractometer (Smartlab, Rigaku Corp., Japan) with a five-axis goniometer and Cu rotating anode generator. A two-bounce Ge (022) monochromator was used for the out-of-plane symmetrical $2\theta/\omega$ scans and rocking curves. Pole figure studies were carried out without the monochromator to assess the in-plane orientation of the multilayers, fixing the 2θ position to a reflection of interest and scanning the χ axis from 0° to 90° and the φ axis from 0° to 360° . For the pole figures, scans around the PCO, STO, and substrate peaks were all carried out from the same multilayer without removing it from the diffractometer, such that the position of the peaks in the φ axis could be compared. The oxygenation bond lengths in the multilayers were investigated using Raman spectroscopy (inVia Raman Microscope, Renishaw, U.K.) using a 532 nm laser source.

Cross-sectional lamellae were prepared for transmission electron microscopy (TEM) via the "lift-out" technique using a dual-beam focused ion beam/scanning electron microscope (FIB/SEM, Nanolab 600i, FEI Company, USA). Sections were taken from approximately the center of the films from an area underneath one of the Pt electrode fingers used for electrical characterization (see below). The lamellae were prepared and thinned at 30 keV, followed by thinning at 5 kV and then 2 kV to reduce amorphous damage to the lamellae.

The microstructure, orientation, and chemistry of the heterostructures were investigated in a JEM-ARM-200F microscope (JEOL Ltd., Japan), operating at 200 keV, and equipped with Cs correctors on the imaging and probe forming lenses. Electron energy loss spectroscopy (EELS) was performed in scanning TEM (STEM)

mode using a Gatan Imaging Filter (GIF, Gatan Inc., USA) in dual-EELS mode. Energy-dispersive X-ray spectroscopy (EDXS) was carried out using an SDD-type X-ray detector (solid angle of 0.8 sr).

2.3. Electrical Characterization. The conductivity of the multilayers was measured using ~ 200 nm-thick Pt-interdigitated electrodes deposited on the surface using DC sputtering (TS-DC.RF303, Pascal Corp., Japan). The electrode geometry was defined using a shadow mask with an electrode width of $220\ \mu\text{m}$ and spacing of $180\ \mu\text{m}$ as measured by an optical microscope. Ag wires were attached to the electrodes using Ag paint and annealed at $250\ ^\circ\text{C}$ to ensure good electrical and mechanical contact. To check for any artifacts in the conductivity from the top electrode geometry, a $(20 + 20) \times 5$ multilayer sample was also scratched down to the substrate in two places and Pt sputtered into the scratches such that all layers were directly in contact with the electrodes (shown in Figure S11 in the Supporting Information).

The multilayers were positioned in a tubular furnace using a custom-made sample holder with a thermocouple positioned directly adjacent to the sample. The P_{O_2} was controlled using an O_2/N_2 mix using mass flow controllers and monitored using a YSZ Nernst-type oxygen sensor. The in-plane conductivity was measured in a range of 500 to $650\ ^\circ\text{C}$ using two-point impedance measurements (Alpha-A Frequency Analyzer, Novocontrol Technologies GmbH & Co., KG, Germany), with a frequency range of $1\ \text{MHz}$ to $0.1\ \text{Hz}$, zero DC bias, and an amplitude of $1\ \text{V}$. The resultant impedance spectra were fitted using the Z-View software (Scribner Associates, USA).

2.4. Optical Transmission Measurements. The total transmission of the multilayer samples was measured normal to the surface as a function of P_{O_2} by a custom-made dual-beam spectrophotometer. A monochromatic light beam ($2\ \text{nm}$ linewidth) was passed through the samples positioned within a quartz cell installed inside a furnace heated to 550 – $650\ ^\circ\text{C}$. The temperature was measured using a thermocouple adjacent to the sample in the furnace, and the P_{O_2} varied using O_2/Ar and $\text{H}_2/\text{H}_2\text{O}/\text{Ar}$ mixtures with the aid of mass flow controllers. A beam splitter was used to direct part of the incident beam to a reference sample (MgO substrate) positioned next to the multilayer sample in the optical cell, which allowed for the removal of variations in the light source intensity, optical noise from the furnace, and artifacts as the beam passes through the quartz tube and substrate. To improve the signal-to-noise ratio, the incident beam was mechanically chopped at constant frequency and then measured using a lock-in amplifier (SRS, model SR830). The incident beam wavelength could be scanned over a range of 350 to $1100\ \text{nm}$ (Newport Apex Illuminator 70613NS with monochromator 74100) to obtain a continuous optical transmission spectrum.

To extract the optical absorption coefficient of Pr^{4+} ions, spectra were obtained over the full wavelength range for various oxygen partial pressures, and the wavelengths at which the transmission is most sensitive to changes in Pr^{4+} concentration were identified. It was found that the largest change in transmission with P_{O_2} due to a wideband absorption peak, occurs at a wavelength of around $470\ \text{nm}$, as shown in Figure S12a in the Supporting Information. The absorption spectrum displaying a broad absorption peak around $470\ \text{nm}$ is characteristic to PCO as verified on a $100\ \text{nm}$ -thick epitaxial PCO film. Changes in transmission were measured at constant wavelengths of $480\ \text{nm}$ for the $(100 + 100) \times 1$ sample and $470\ \text{nm}$ for the $(5 + 5) \times 20$ sample as a function of P_{O_2} (Figure S12b in the Supporting Information) and the total optical absorption coefficient, α , calculated according to eq 5. To extract the partial optical absorption coefficient due to Pr^{4+} , $\alpha_{\text{Pr}^{4+}}$, according to eq 6, the data were normalized to a baseline “transparent” value of α at low P_{O_2} levels (below $10^{-20}\ \text{atm}$), where all the Pr can be assumed to be in the $3+$ valance state and the Pr^{4+} concentration assumed to be negligible.

3. RESULTS

3.1. Orientation and Microstructure. Figure 1a shows XRD $2\theta/\omega$ scans of the PCO/STO multilayer samples, an

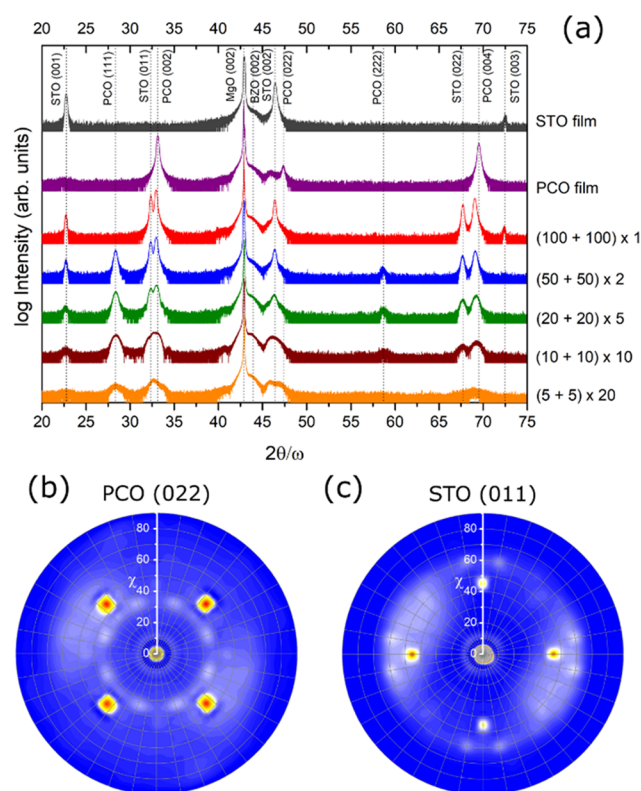


Figure 1. (a) XRD out-of-plane $2\theta/\omega$ scans of the PCO/STO multilayers. The peaks have been indexed and are labeled accordingly. Pole figures of the (b) PCO (022) reflection and the (c) STO (011) reflection are shown below for the $(20 + 20) \times 5$ multilayer.

epitaxial STO film and an epitaxial PCO film, all grown on MgO with the BZO and STO double buffer layer. The epitaxial STO film and PCO film display only peaks corresponding to the (001) planes aligned out-of-plane with the (001) planes of the MgO substrates. For the bilayer sample $((100 + 100) \times 1)$, an additional STO (011) reflection can be observed, suggesting that the (001) oriented epitaxy is not retained for STO layers grown on top of PCO. For the heterostructures with a greater number of layers, another additional set of peaks corresponding to the PCO (111) planes becomes visible. Because PCO will grow epitaxially in the (001) orientation on (001) STO, the results suggest that the PCO with the (111) orientation grows on the STO in the (011) orientation.

Pole figures of a $(20 + 20) \times 5$ multilayer taken at the PCO (022) and the STO (011) Bragg angles are shown in Figure 1b,c, respectively. The PCO (022) pole figure shows two sets of reflections: 4 maxima spaced evenly in the azimuth direction at $\psi \sim 45^\circ$, indicating a single in-plane orientation of the (001) out-of-plane oriented grains, and 12 maxima at $\psi \sim 35.3^\circ$, signifying four in-plane orientations of the PCO grains oriented (111) out-of-plane. The STO (011) pole figure also displays two sets of reflections: four maxima at $\psi \sim 45^\circ$, representing a single in-plane orientation of the (001) oriented grains, and eight maxima at $\psi \sim 60^\circ$ grouped in pairs, indicating two in-plane orientations of the (011) out-of-plane oriented grains.

Based on the analysis of the $2\theta/\omega$ scans and pole figures, the orientation relationships of the heterostructures can be inferred. Figure 2 shows the orientation of the PCO and STO layers schematically. Epitaxy is clearly maintained from the MgO substrate, through the BZO and STO buffer layers,

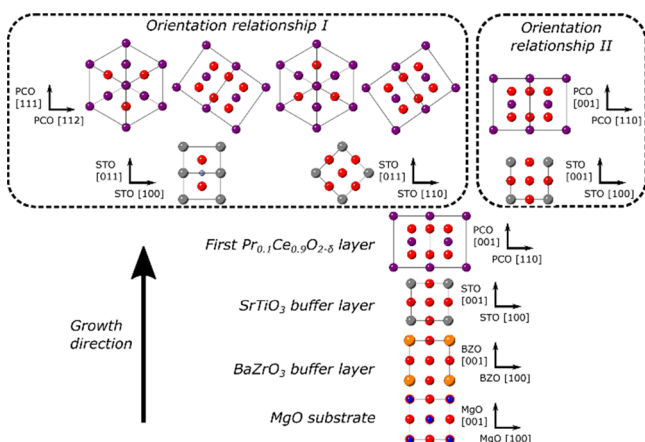


Figure 2. Schematic diagram of the orientation relationships for the PCO/STO multilayers. The orientation from the MgO substrate through the two buffer layers and the first PCO layer is shown after which two orientation relationships of the PCO/STO develop.

and into the first PCO layer. From here, the STO can remain in the (001) out-of-plane orientation, which should result in the PCO grown on top in the same orientation, maintaining the epitaxial relationship. Alternatively, if grains of the STO grown on the PCO in the (011) out-of-plane orientation, then the PCO orientation also changes, and (111) oriented PCO grains will grow.

Figure 3 shows rocking curves taken from the PCO (002) reflection of the heterostructures. A clear broadening of the

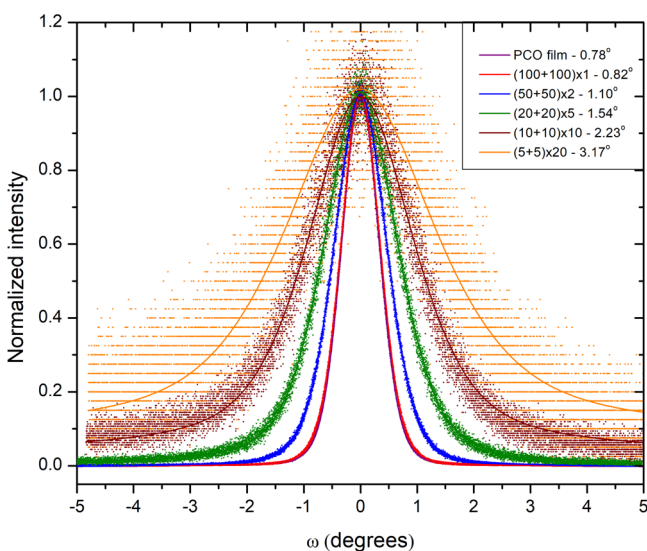


Figure 3. Intensity-normalized rocking curves of the PCO (002) reflection of the PCO/STO multilayer films. The data have been fitted with a pseudo-Voigt function, and the full-width-half-maximum values are given in the legend. The grouping of the data into horizontal lines for the $(5+5) \times 20$ sample is an artifact due to the counting statistics of the XRD scintillator detector.

peaks is seen as the thickness of the layers decreases and the total number of layers increases. Broadening of the peak width in rocking curves may be caused by an increased mosaic spread or tilting of the grains, decreasing layer thickness or decreasing grain size, and an increase in defects such as dislocations.⁴³ From the TEM analysis discussed below, a decreasing grain size is observed as the thickness of the layers is decreased,

which is consistent with the broadening of the rocking curves peaks in Figure 3.

The out-of-plane lattice parameters extracted from the peak positions of the $2\theta/\omega$ scans are shown in Figure 4. All films

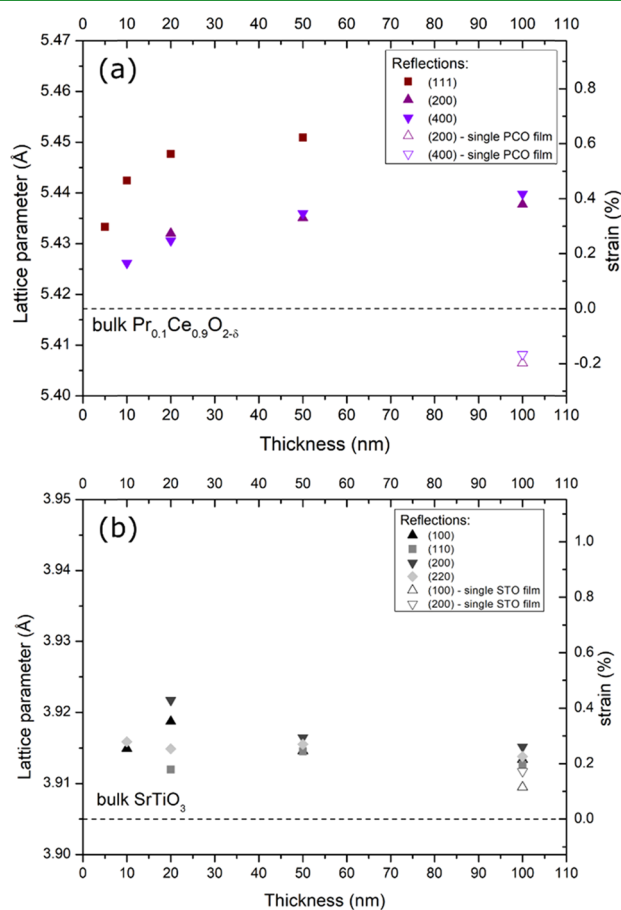


Figure 4. Out-of-plane lattice parameters extracted from the peak position of the $2\theta/\omega$ scans for (a) the PCO reflections and (b) the STO reflections. Bulk values refer to those measured on the pellets used as PLD targets.

were annealed in flowing synthetic air at 700 °C for 2 h after growth, and therefore, the nonstoichiometry should be in equilibrium with atmospheric conditions. The lattice parameters for STO showed a slight expansion of approximately 0.2% in comparison to the bulk ceramic, whereas the PCO lattice parameters show a much more substantial deviation. A PCO epitaxial film is approximately 0.2% smaller than expected from the parameters on the parent PCO target, while the multilayer samples all show an increase in lattice parameter. There is also a discrepancy between the lattice parameters taken from the {001} family of planes and from the (111) peaks.

The oxygen-cation bond lengths of CeO_2 can be directly probed using Raman spectroscopy to confirm the changes in the lattice parameter.^{16,44} Raman spectra of the multilayers are shown in Figure S1 in the Supporting Information. The peak at $\sim 460 \text{ cm}^{-1}$ is assigned to the Ce–O stretching mode with F_{2g} symmetry,⁴⁵ and the broad peak at $\sim 570 \text{ cm}^{-1}$ is due to a Raman resonance effect caused by Pr^{4+} -containing defects and the absorption band at around 530 nm.⁴⁶ The peak position of the F_{2g} mode is related to the Ce–O bond length and is plotted in Figure S2 as a function of layer thickness, demonstrating a redshift to lower wavenumbers with

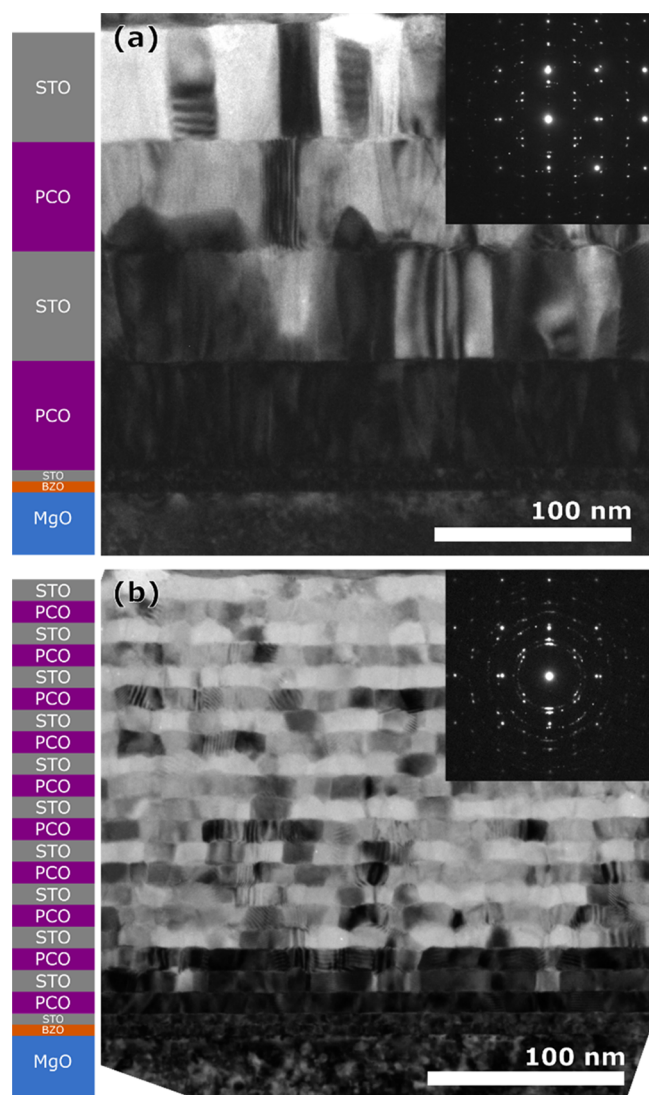


Figure 6. Bright field TEM images of a (a) $(50 + 50) \times 2$ multilayer and (b) $(10 + 10) \times 10$ multilayer. The diffraction contrast clearly highlights the grains and microstructure. The SAED patterns of a region contained the full thickness of the film and part of the substrate are shown in the insets. The SAED patterns have been indexed and are shown in Figure S5 in the Supporting Information.

fringes are also visible, caused by overlapping grains with distinct orientations within the thickness of the lamella sample. The grain size decreases from approximately 25 nm for the 50 nm layer thickness to around 15 nm for the 10 nm layer thickness.

The insets in Figure 6 display the selected area electron diffraction (SAED) patterns of a region containing the full multilayers and part of the substrate. The indexed patterns are shown in Figure S5 in the Supporting Information and confirm the orientation relationships shown in Figure 2. This was further confirmed from high-resolution HAADF-STEM imaging as exemplified in Figure 7. As inferred from the XRD analysis, the first layer of the PCO grows epitaxially in the (001) out-of-plane direction, whereas the subsequent STO layer may either grow in the (001) or (011) orientation, as seen in the micrograph. It can be clearly observed that if the (001) epitaxy is maintained for a grain of the STO layer, then the following PCO grain growing directly on top also remains

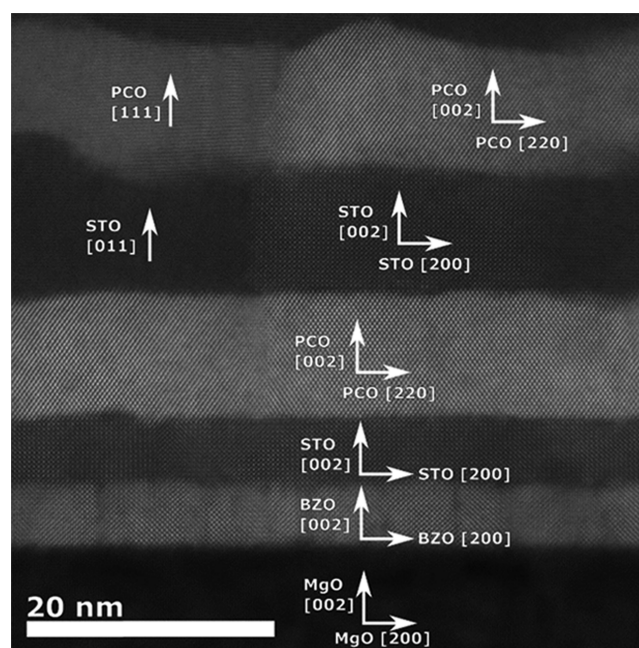


Figure 7. High-resolution HAADF-STEM image of the first layers of a $(10 + 10) \times 10$ multilayer. The different orientation relationships inferred from the XRD data and displayed in Figure 2 can be seen in the lattice image.

in the (001) orientation, whereas for STO grains that switch to the (011) orientation, the subsequent PCO will switch to the (111) out-of-plane orientation.

An increased roughness of the layers is observed after the first or second PCO layer in the growth direction. Rare-earth-substituted ceria has been reported to grow in the island or Volmer–Weber mode on STO surfaces.⁵⁰ The changes in orientation are presumably caused by the minimization of the surface energies between the PCO/STO interfaces and the PCO and STO surfaces with the gas phases. As the PCO and STO orientation changes with increasing number of layers, as illustrated in Figure 2, faceting of the grains starts to take place to reduce the interfacial energy at the gas/solid interface. This may be the reason for the increased roughness, which is often observed in multilayers as the number of layers increases.^{51–53} In this case, it is not observed to be extreme enough to lead to any discontinuation of the layers.

Recently, there have been reports of dramatically reduced ceria or rare-earth-substituted ceria where a substantial amount of Ce is reduced from Ce^{4+} to Ce^{3+} at either heterogeneous interfaces,^{54,55} grain boundaries,³⁸ or due to lattice strain.⁵⁶ To investigate the possible reduction of Ce in the multilayers, EELS line scans were performed on the samples, as shown in Figure 8. It has been shown elsewhere^{54,57} that the Ce $\text{M}_{4,5}$ edge shows three distinct changes as the valence state of Ce is reduced from Ce^{4+} to Ce^{3+} : (1) the edge onsets shift to lower energy, (2) the ratio of the intensity of the peaks (Ce $\text{M}_5/\text{Ce} \text{M}_4$) changes (<1 for Ce^{4+} and >1 for Ce^{3+}), and (3) the high energy shoulder on the Ce M_5 and Ce M_4 edges disappears. It should be noted that the Pr $\text{M}_{4,5}$ edge also displays the same changes as Pr reduces from Pr^{4+} to Pr^{3+} , but unfortunately reduction occurs readily under the electron beam,⁵⁸ and it was always observed in the Pr^{3+} state.

EELS spectra are given in Figure 8, taken from selected points from a line scan across layers of a $(10 + 10) \times 10$

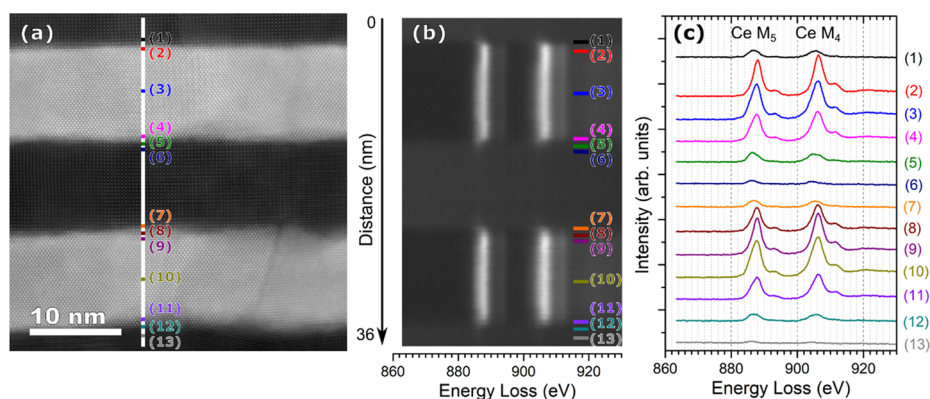


Figure 8. EELS line scan across the layers of a $(10 + 10) \times 10$ heterostructure. (a) An HAADF-STEM image with the position of the probe as it scans across the PCO and STO layers. (b) The spectrum image during the acquisition and (c) the spectra from selected points during the line scan, which show the change in the Ce $M_{4,5}$ edge.

heterostructure. No significant reduction of the Ce is observed within the PCO layers. A shift in the edge energy and change in the ratio of the edge intensity is seen when the electron probe is directed adjacent to the PCO layer (in positions (1), (5), (7), and (12) in Figure 8); however, this is more consistent with a slight interdiffusion of Ce into the STO layer, in a 3+ valence state. Alternatively, delocalization effects whereby the EELS signal originates from outside the electron probe would also explain these observations. Further EELS line scans of the $(50 + 50) \times 2$ and across grain boundaries are shown in the Supporting Information (Figures S6 and S7), where no evidence of Ce reduction in the PCO layers was observed.

3.2. Transport Properties. The electrical conductivities of the multilayers are shown in Figure 9, as a function of P_{O_2} for two temperatures. Typical Nyquist plots and data collected for each sample over the full temperature range (500–650 °C) are shown in Figures S8 and S9 in the Supporting Information, respectively. The conductivity of a single epitaxial STO film is shown in Figure S10 in the Supporting Information for comparison with an epitaxial PCO film, displaying a conductivity several orders of magnitude lower than PCO over the temperature and P_{O_2} range. The lattice parameters of the STO layers indicate that a slight cation nonstoichiometry may be present, which has been reported to decrease the conductivity of STO for both Sr and Ti deficiencies. From Figure 4, it can be seen that the lattice parameters of the multilayer samples and the single STO film show very little variation, and so the conductivity of STO in Figure S10 is expected to be representative of the STO layers in the heterostructures, barring any interface effects.

For a single epitaxial PCO thin film, the conductivity at high oxygen partial pressures displays a slope close to $-1/6$, which is predicted by substituting eq 3 into eq 2 to give $[Pr'_{Ce}] \approx 2[v'_O] \propto P_{O_2}^{-1/6}$. The conductivity agrees well with previous measurements on bulk ceramic PCO,²¹ although it is slightly higher in magnitude. This is most likely due to the lack of grain boundaries in the epitaxial PCO film compared with polycrystalline ceramics.

By comparing between the conductivities of the multilayers in Figure 9, two trends become apparent as the thickness of the layers is decreased. First, there is a significant weakening of the P_{O_2} dependence. Slopes fitted to the data in the high P_{O_2} region in Figure S9 of the Supporting Information show the P_{O_2}

weakening more explicitly. Second, there is an overall decrease in the total magnitude of the conductivity.

First, we discuss the observed weakening of the P_{O_2} dependence. This is consistent with a decrease in reduction enthalpy, $\Delta H_{r, pr}$ in eq 2 and may be thought of as observing the onset of the ionic plateau shifting to higher oxygen partial pressures. This is also supported by the decrease in activation energy at 1 atm, as shown in Figure 10a, which should start to approach the activation energy of oxygen ion hopping in PCO (0.7 eV).²¹ However, as PCO becomes more reduced, total conductivity should increase, yet this is not observed, and instead, as the P_{O_2} dependence becomes lesser for the thinner layers, the total conductivity decreases. This brings us to the cause of the decrease in the conductivity observed for decreasing layer thickness observed in Figure 9.

We can conceive three plausible reasons for the reduced conductivity: (1) there is an increasing density of grain boundaries as the number of layers in the heterostructures increases, (2) due to the electrical contacts being placed on the surface of the sample, the increased number of PCO/STO interfaces prevents the current during electrical testing from uniformly flowing through the full multilayer, or (3) a combination of both grain boundaries and blocking interfaces.

From the microstructural data obtained by TEM, there is a decrease in grain size as the thickness of the individual layers decreases (as seen in Figure 6). Furthermore, the increase in the activation energy at the lowest P_{O_2} , where it is closest to a pure ionic conductor, is consistent with a decrease in the grain size as the total conductivity is increasingly dominated by grain boundaries that are known to have a higher activation energy than the grain core.⁵⁹ Similar changes in the activation energy have been seen in $Gd_{0.1}Ce_{0.9}O_{2-\delta}$ films as a function of grain size.⁶⁰

To check the effect of blocking PCO/STO interfaces, a $(20 + 20) \times 5$ multilayer was measured using both top interdigital finger electrodes, and “side” electrodes, where the multilayer film was scratched using a diamond-tipped scribe down to the substrate in two places and Pt sputtered into the scratches such that all the layers were in contact with the Pt as shown in Figure S11 in the Supporting Information. The resultant electrical measurements display a slight enhancement in conductivity, indicating that PCO/STO interfaces are indeed blocking; however, the enhancement in conductivity is not enough to account for the total decrease when compared to

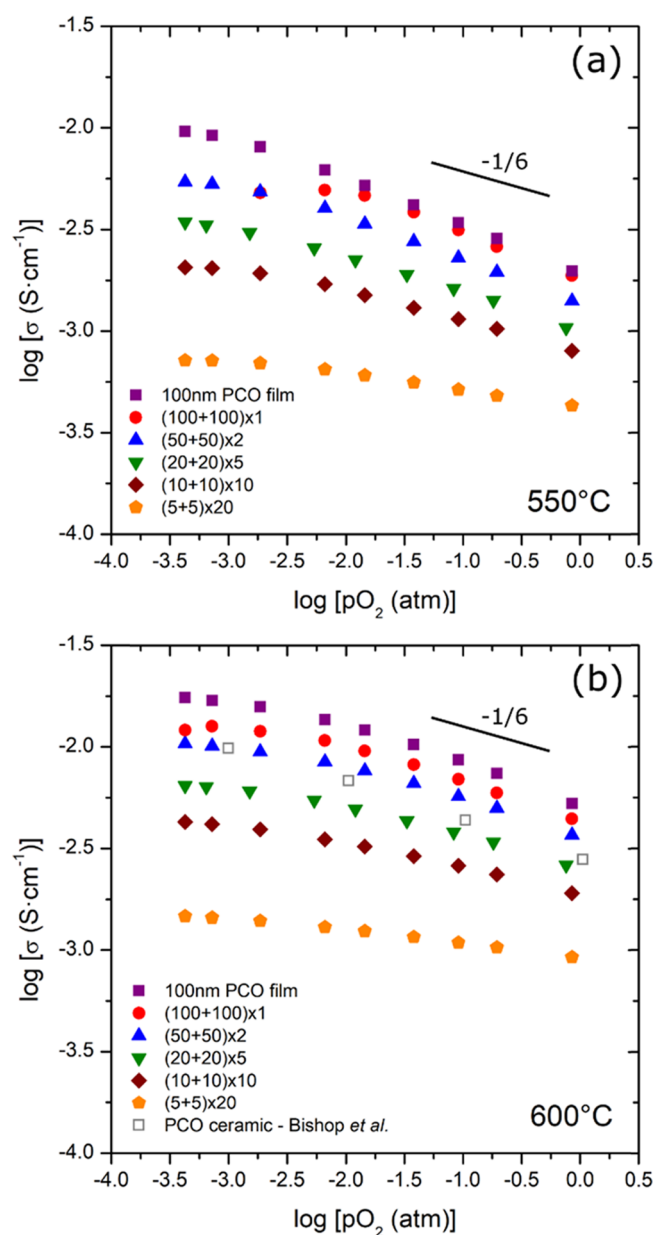


Figure 9. Conductivity of the multilayers as a function of P_{O_2} for (a) 550 °C and (b) 600 °C. The conductivity of ceramic PCO at 600 °C as reported by Bishop et al.²¹ is displayed for comparison.

single PCO films. Therefore, we conclude that a combination of both the increasing density of grain boundaries and PCO/STO interfaces is the cause of the decreased conductivity.

3.3. Optical Properties. One limitation of conductivity ($\sigma_{\text{tot}} = \sum_i [i] z_i q \mu_i$, where $[i]$ is the concentration, z_i is the valence number, and μ_i is the electrical mobility of species i , and q is the elementary charge) measurements on mixed conductors is the difficulty in deconvoluting changes in the charge carrier concentrations ($[Pr_{Ce}']$, $[V_{O}^{\bullet}]$) from changes in the overall mobility of the charge carriers due to grain boundaries or interfaces. To ensure that by confining PCO in the form of multilayers with STO, we are able to tailor $\Delta H_{r,Pr}$, we performed optical transmission measurements on the multilayers. According to eqs 5 and 6, transmitted light intensity can be directly related to the Pr^{4+} concentration via a molar extinction coefficient, $\epsilon_{Pr^{4+}}$.

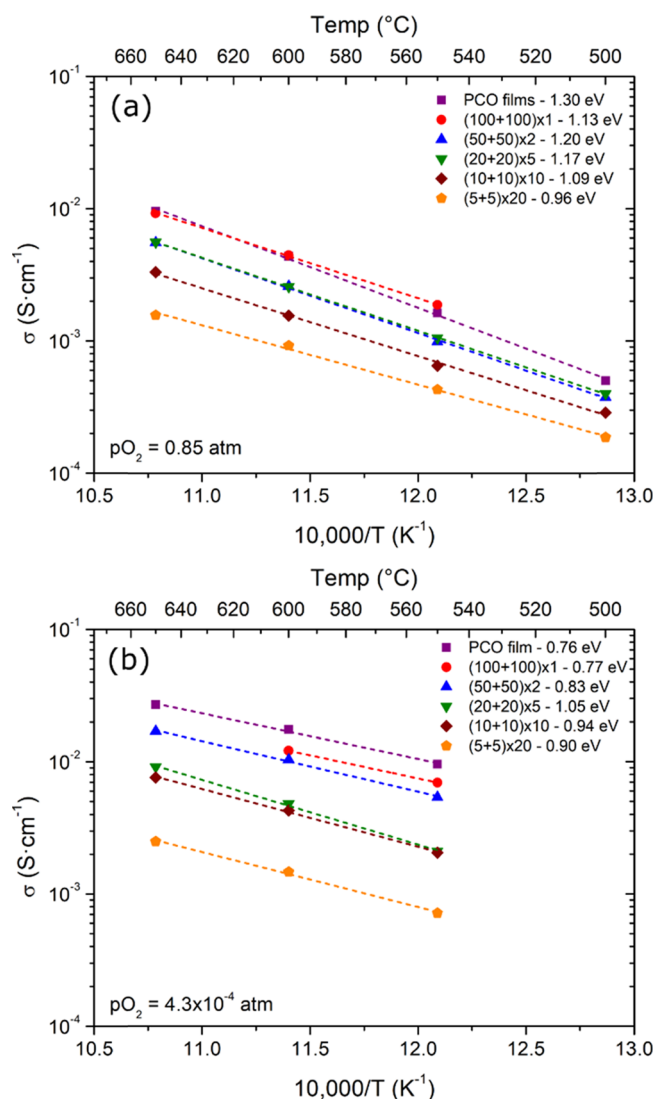


Figure 10. Arrhenius plots showing the activation energy of conductivity of the multilayers for (a) the “mixed ionic electronic conducting region” at high P_{O_2} and (b) the “ionic region” at lowest measured P_{O_2} . The data at 500 °C at the lowest measured P_{O_2} has been omitted as the multilayers had not reached equilibrium with the gas phase. Given the limited number of data points, the activation energies displayed in the legend should be taken as an estimation.

Figure 11a shows the absorption coefficient due to Pr^{4+} ions, $\alpha_{Pr^{4+}}$, as a function of P_{O_2} for heterostructures with 100 and 5 nm layer thicknesses. Transmittance spectra and transients as a function of P_{O_2} are shown in Figure S12 in the Supporting Information. At an oxygen partial pressure of $\sim 10^{-3}$ atm and at 650 °C, $\alpha_{Pr^{4+}}$ is approximately equal for both layer thicknesses. At low oxygen partial pressures and high temperatures, PCO reduces and hence displays the lowest absorption coefficient. Whereas the heterostructure with a 100 nm layer exhibits a significant increase in the absorption coefficient with increases in P_{O_2} , the effect for the heterostructure with 5 nm layer thicknesses shows a much smaller increase. This implies that the heterostructure with thinner layers remains much more reduced at higher oxygen partial pressures. Furthermore, the (5 + 5) × 20 multilayer shows almost no temperature dependence in comparison to the (100 + 100) × 1 multilayer, again

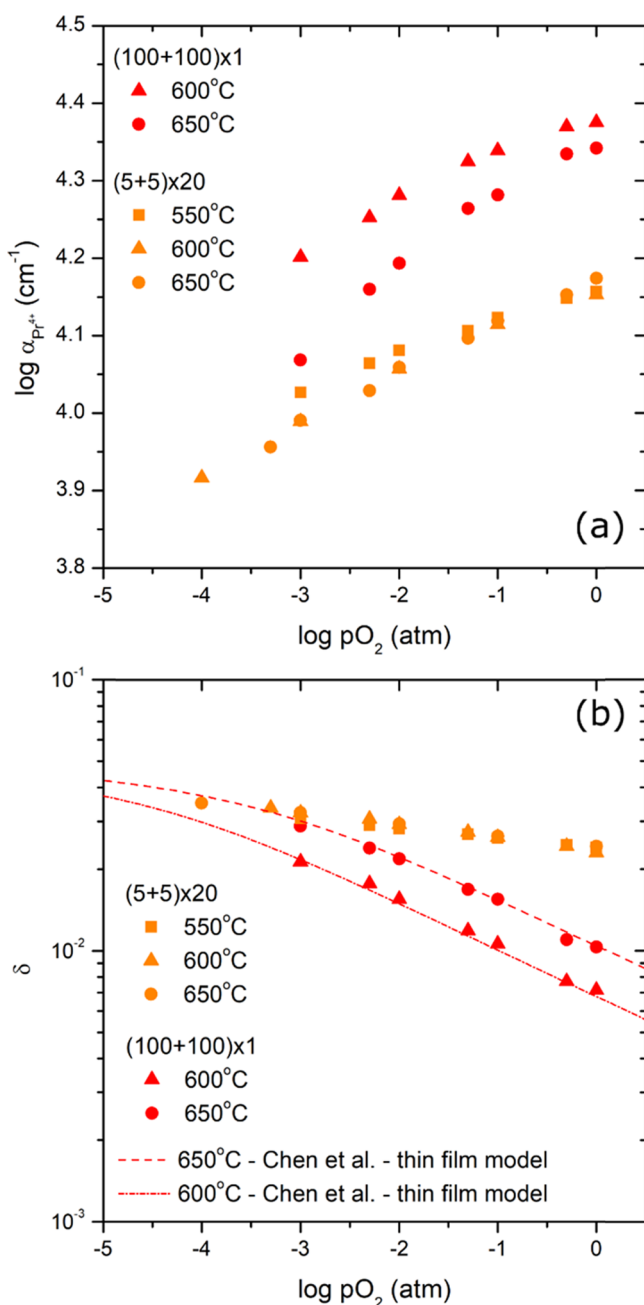


Figure 11. (a) Absorption coefficient, $\alpha_{Pr^{4+}}$, and (b) the extracted nonstoichiometry, δ , of a $(100 + 100) \times 1$ multilayer and a $(5 + 5) \times 20$ multilayer as a function of P_{O_2} . The dashed lines in (b) represent the defect model reported for thin-film PCO by Chen and Tuller.²⁷

consistent with a Pr^{3+} concentration, which remains fixed to a greater degree.

Although a promising approach, the optical measurements are very sensitive to changes in the reference point, where the $[Pr^{4+}]$ is independently known for some absorption coefficient and molar extinction coefficient. The latter requires an independent technique for measuring the Pr^{4+} concentration, for example, based on chemical capacitance measurements.²⁷ In this study, the nonstoichiometry calculated according to eq 6 is plotted in Figure 11b, where $\epsilon_{Pr^{4+}}$ was calculated for the $(100 + 100) \times 1$ multilayer by fitting the data at 1 atm to the defect model reported by Chen and Tuller in PCO films based on chemical capacitance measurements.²⁷ A value of $1.1 \times$

10^{-17} cm^2 for $\epsilon_{Pr^{4+}}$ was obtained, which is in reasonable agreement with those values previously reported by Kim et al.^{24,28} considering the different experimental setup and slightly different wavelength used (480 and 470 nm in this work compared to 532 nm). From Figure 11b, the nonstoichiometry for the heterostructure with 100 nm thick layers is in excellent agreement with literature values over the full P_{O_2} range. When calculating the nonstoichiometry for the $(5 + 5) \times 20$ multilayer using the same value for $\epsilon_{Pr^{4+}}$, clearly, the slope becomes much shallower, in accordance with the conductivity data for the same structure and consistent with higher oxygen deficiency at higher oxygen partial pressures.

4. DISCUSSION

As discussed above, the weakening of the P_{O_2} dependence and changes in activation energy are consistent with a decrease in $\Delta H_{r, Pr}$ of the multilayers in comparison with either thin film or ceramic PCO, which becomes more severe for thinner, more confined layers. We conclude that both blocking PCO/STO interfaces and grain boundaries are the most likely cause of the overall decrease in the magnitude of the conductivity, but, from the optical measurements, we can rule out the observed P_{O_2} weakening as an artifact of transport across blocking boundaries in the samples. In a separate study comparing between epitaxial and polycrystalline films with different grain boundary densities, we demonstrate only a slight decrease in the conductivity and no significant weakening of the P_{O_2} dependence.⁶¹ This indicates that the PCO/STO interfaces are the primary cause of the observed decrease in $\Delta H_{r, Pr}$.

Although the observed changes in the multilayers are consistent with a decrease in $\Delta H_{r, Pr}$, it seems unlikely that $\Delta H_{r, Pr}$ is modified uniformly across the layers of each heterostructure. While such size-dependent changes in the thermodynamic properties have been reported, they typically occur for materials in which a majority of the volume fraction can be considered part of the surface (within 0.5 nm).⁶² In the PCO multilayers, the weakening of the P_{O_2} dependence becomes apparent for the structures with a layer thickness of $<100 \text{ nm}$ and becomes more extreme with decreasing layer thickness, which is more consistent with an interface proximity effect. Indeed, similar changes in the electrical properties of STO films under reducing conditions have been described in such a manner.⁶³

Assuming the nonstoichiometry of PCO is not constant across the layers, there are two possible scenarios: (1) Due to excess charge at the interfaces, space charge layers form adjacent to the interfaces where charge carriers are either accumulated or depleted, and local charge neutrality is not obeyed. (2) $\Delta H_{r, Pr}$ varies as a function of distance from the interface, and charge neutrality is conserved according to eq 3.

For the most part, quantitatively describing space charge layers has been reserved for systems within the dilute limit. When calculating the Debye length for PCO, which is of the order of magnitude of the width of a space charge zone, one obtains a width that is within a few nanometers; however, by including either defect–defect interactions¹⁷ or mechanical effects,¹⁸ recent theoretical work has predicted more substantial widths. At high P_{O_2} , when $[Pr'_{Ce}] \ll [Pr^x_{Ce}]$, both Pr'_{Ce} and \bar{v}_O may be thought of as mobile charge carriers, and the situation becomes similar to a Gouy–Chapman model in the dilute limit. Usually, grain boundaries in CeO_2 -based solid

solutions contain excess positive charge due to a reduction in v_{O} formation energy within the core, and so if we were to assume this was the same for the PCO/STO interface, we would expect to see a simultaneous enrichment of Pr'_{Ce} and a depletion of v_{O} . At lower P_{O_2} , when $[\text{Pr}'_{\text{Ce}}] \approx [\text{Pr}'_{\text{Ce}}]_{\text{total}}$, the situation becomes similar to a Mott–Schottky situation, where the $[\text{Pr}'_{\text{Ce}}]$ remains constant up to the interface, and the excess charge in the core is accounted for solely by a depletion of v_{O} .

Considering conduction parallel to the PCO/STO interfaces only, these space charge effects may lead to an enhancement of polaron hopping at high P_{O_2} and a decrease in oxygen-ion migration over the full P_{O_2} range, which could lead to the observed weakening of the P_{O_2} dependence. However, considering the uncertainty due to the transport across the PCO/STO interfaces and the presence of grain boundaries, attempting to fit a dilute model for space charge zones to the conductivity data would be of limited use. Both Bowman et al.³⁸ and Swallow et al.³⁵ investigated grain boundaries and interfaces in Pr/Gd-codoped and Pr-doped CeO_2 , respectively, using EELS. Bowman et al. reported an enrichment of Pr over Gd at the grain boundary, and Swallow et al. reported an increase in Pr'_{Ce} at the YSZ substrate interface, although neither work explicitly demonstrated that oxygen was accumulated at the boundaries, in accordance with a space charge effect, rather than depleted according to the electroneutrality condition.

Instead, we may consider that $\Delta H_{\text{r, Pr}}$ varies in proximity to the interface, and that eq 3 is upheld. There are several reasons one may expect $\Delta H_{\text{r, Pr}}$ to vary due to interfacial effects. The first is due to mechanical clamping of the PCO at the PCO/STO interface. Chemical expansion of STO should be negligible compared to PCO within the P_{O_2} range and temperatures investigated here, and hence, a mechanical coupling of the two materials at the interface may restrict the ability of PCO to freely expand as it would in ceramic form. Indeed, in situ TEM measurements on the interface of PCO and YSZ, another relatively inert material, have shown that chemical expansion is reduced in directions parallel to the interface plane and enhanced in directions perpendicular to it.³⁵

Second, from the lattice mismatches calculated for the orientation relationships for the PCO/STO interfaces, in some cases, the mismatch is small enough ($\sim 2\%$) that one might expect a coherent interface to form, inducing a tensile strain in PCO. Gopal et al. have shown that tensile (and compressive) strain in CeO_2 films dramatically increases their oxygen storage capacity due to, in part, a reduced oxygen vacancy formation energy with biaxial tensile strain.⁵⁶ For perovskite-based oxide thin films, changes in the nonstoichiometry due to an applied lattice strain have also been reported.⁶⁴

Finally, other orientation relationships for the PCO/STO multilayers yield huge mismatches ($f_{\text{PCO/STO}} > \pm 15\%$), which would undoubtedly lead to either incoherent interfaces or high densities of dislocations. In rare-earth-substituted CeO_2 , dislocations have been both experimentally³⁵ and computationally⁶⁵ observed to act as traps for reduced cations and oxygen vacancies.

At this point, we are not able to give a conclusive statement on whether space charge effects dominate the properties of PCO/STO multilayers or rather if $\Delta H_{\text{r, Pr}}$ varies as a function of the proximity to the interface. However, we have demonstrated that the properties of PCO, a model mixed

ionic electronic conductor, can be tailored through interface effects. By simply changing the layer thickness in the multilayer, something easily modified during thin-film deposition methods, we have been able to dramatically alter the effective enthalpy of reduction and hence the nonstoichiometry in PCO.

5. CONCLUSIONS

The effect of confinement on the electrical properties of PCO has been studied in heterostructures with STO as grown by PLD. By keeping the total thickness constant, while the thickness of each layer and the number of layers were simultaneously changed, the total volume of PCO and STO remained the same but the interface density was varied. Two trends in the conductivity of the multilayers were observed as the thickness of the layers was decreased: a weakening of the P_{O_2} dependence and a decrease in the total magnitude of the conductivity. We conclude that the decrease in the magnitude of the conductivity is due to blocking PCO/STO interfaces and grain boundaries perpendicular to the current direction, and that the weakening of the P_{O_2} dependence is caused by a decrease in the effective reduction enthalpy. This was confirmed through optical absorption measurements performed in situ as a function of temperature and P_{O_2} .

These results demonstrate the potential for tailoring the nonstoichiometry of mixed ionic and electronic conducting oxides through interface engineering. By varying the interface density in multilayer structures, we have demonstrated significant changes in the functional properties of PCO, which provides valuable information toward developing electroceramics at the nanoscale for a wide variety of applications.

■ ASSOCIATED CONTENT

Supporting Information

The Supporting Information is available free of charge on the ACS Publications website at DOI: 10.1021/acsami.9b08864.

Details of the calculated lattice mismatches; Raman spectra (S1) and Raman shifts (S2); STEM-EDX elementary maps (S3); STEM-EELS compositional line scans (S4); indexed SAED patterns (S5); STEM-EELS Ce valence line scans (S6 and S7); EIS Nyquist plots (S8); conductivities of the multilayers (S9); comparison of PCO and STO epitaxial film conductivities (S10); comparison of “top” IDE and “side” electrodes on the conductivity (S11); optical transmission spectra and transients as a function of P_{O_2} (S12) (PDF)

■ AUTHOR INFORMATION

Corresponding Author

*E-mail: harrington.frederick.george.302@m.kyushu-u.ac.jp.

ORCID

George F. Harrington: 0000-0001-5641-3304

Bilge Yildiz: 0000-0002-2688-5666

Nicola H. Perry: 0000-0002-7207-2113

Notes

The authors declare no competing financial interest.

ACKNOWLEDGMENTS

G.F.H. gratefully acknowledges financial support from a Kakenhi Grant-in-Aid for Encouragement of Young Scientists (B) Award (no. JP18K13992) and the Platform of Inter/Transdisciplinary Energy Research Support Program (Q-pit) at Kyushu University. The authors are also grateful for support from the Progress 100 program of Kyushu University and the International Institute for Carbon-Neutral Energy Research (WPI-I2CNER), both supported by MEXT, Japan, and the Center of Innovation Science and Technology based Radical Innovation and Entrepreneurship Program (COI Program) and by the Japan Science and Technology Agency (JST) (grant no. JPMJCE1318). D.K., H.L.T., and B.Y. acknowledge support for their research from the Department of Energy, Basic Energy Sciences under award no. DE-SC0002633 (Chemomechanics of Far-From-Equilibrium Interfaces).

REFERENCES

- (1) Steele, B. C. H.; Heinzel, A. Materials for Fuel-Cell Technologies. *Nature* **2001**, *414*, 345–352.
- (2) Skinner, S. J.; Kilner, J. A. Oxygen Ion Conductors. *Mater. Today* **2003**, *6*, 30–37.
- (3) Ni, M.; Leung, M. K. H.; Leung, D. Y. C. Technological Development of Hydrogen Production by Solid Oxide Electrolyzer Cell (SOEC). *Int. J. Hydrogen Energy* **2008**, *33*, 2337–2354.
- (4) Dyer, P. Ion Transport Membrane Technology for Oxygen Separation and Syngas Production. *Solid State Ionics* **2000**, *134*, 21–33.
- (5) Miura, N.; Sato, T.; Anggraini, S. A.; Ikeda, H.; Zhuiykov, S. A Review of Mixed-Potential Type Zirconia-Based Gas Sensors. *Ionics* **2014**, *20*, 901–925.
- (6) Waser, R.; Aono, M. Nanoionics-Based Resistive Switching Memories. *Nat. Mater.* **2007**, *6*, 833–840.
- (7) He, L.; Vanderbilt, D. First-Principles Study of Oxygen-Vacancy Pinning of Domain Walls in PbTiO_3 . *Phys. Rev. B* **2003**, *68*, 134103.
- (8) Li, M.; Pietrowski, M. J.; De Souza, R. A.; Zhang, H.; Reaney, I. M.; Cook, S. N.; Kilner, J. A.; Sinclair, D. C. A Family of Oxide Ion Conductors Based on the Ferroelectric Perovskite $\text{Na}_{0.5}\text{Bi}_{0.5}\text{TiO}_3$. *Nat. Mater.* **2014**, *13*, 31–35.
- (9) Bishop, S. R.; Perry, N. H. *Electro- Chemo- Mechanics of Solids*; Bishop, S. R., Perry, N. H., Marrocchelli, D., Sheldon, B. W., Eds.; Springer: Cham, Switzerland, 2017.
- (10) Litzelman, S. J.; Hertz, J. L.; Jung, W.; Tuller, H. L. Opportunities and Challenges in Materials Development for Thin Film Solid Oxide Fuel Cells. *Fuel Cells* **2008**, *8*, 294–302.
- (11) Yang, J. J.; Strukov, D. B.; Stewart, D. R. Memristive Devices for Computing. *Nat. Nanotechnol.* **2013**, *8*, 13–24.
- (12) Fortunato, E.; Ginley, D.; Hosono, H.; Paine, D. C. Transparent Conducting Oxides for Photovoltaics. *MRS Bull.* **2007**, *32*, 242–247.
- (13) Eranna, G.; Joshi, B. C.; Runthala, D. P.; Gupta, R. P. Oxide Materials for Development of Integrated Gas Sensors—A Comprehensive Review. *Crit. Rev. Solid State Mater. Sci.* **2004**, *29*, 111–188.
- (14) Korte, C.; Keppner, J.; Peters, A.; Schichtel, N.; Aydin, H.; Janek, J. Coherency Strain and Its Effect on Ionic Conductivity and Diffusion in Solid Electrolytes – an Improved Model for Nanocrystalline Thin Films and a Review of Experimental Data. *Phys. Chem. Chem. Phys.* **2014**, *16*, 24575–24591.
- (15) Harrington, G. F.; Cavallaro, A.; McComb, D. W.; Skinner, S. J.; Kilner, J. A. The Effects of Lattice Strain, Dislocations, and Microstructure on the Transport Properties of YSZ Films. *Phys. Chem. Chem. Phys.* **2017**, *19*, 14319–14336.
- (16) Harrington, G. F.; Sun, L.; Yildiz, B.; Sasaki, K.; Perry, N. H.; Tuller, H. L. The Interplay and Impact of Strain and Defect Association on the Conductivity of Rare-Earth Substituted Ceria. *Acta Mater.* **2019**, *166*, 447–458.
- (17) Mebane, D. S.; De Souza, R. A. A Generalised Space-Charge Theory for Extended Defects in Oxygen-Ion Conducting Electrolytes: From Dilute to Concentrated Solid Solutions. *Energy Environ. Sci.* **2015**, *8*, 2935–2940.
- (18) Vikrant, K. S. N.; Chueh, W. C.; García, R. E. Charged Interfaces: Electrochemical and Mechanical Effects. *Energy Environ. Sci.* **2018**, *11*, 1993–2000.
- (19) Bishop, S. R.; Stefanik, T. S.; Tuller, H. L. Defects and Transport in $\text{Pr}_x\text{Ce}_{1-x}\text{O}_{2-\delta}$: Composition Trends. *J. Mater. Res.* **2012**, *27*, 2009–2016.
- (20) Bishop, S. R.; Tuller, H. L.; Kuru, Y.; Yildiz, B. Chemical Expansion of Nonstoichiometric $\text{Pr}_{0.1}\text{Ce}_{0.9}\text{O}_{2-\delta}$: Correlation with Defect Equilibrium Model. *J. Eur. Ceram. Soc.* **2011**, *31*, 2351–2356.
- (21) Bishop, S. R.; Stefanik, T. S.; Tuller, H. L. Electrical Conductivity and Defect Equilibria of $\text{Pr}_{0.1}\text{Ce}_{0.9}\text{O}_{2-\delta}$. *Phys. Chem. Chem. Phys.* **2011**, *13*, 10165–10173.
- (22) Kuru, Y.; Bishop, S. R.; Kim, J. J.; Yildiz, B.; Tuller, H. L. Chemomechanical Properties and Microstructural Stability of Nanocrystalline Pr-Doped Ceria: An in Situ X-Ray Diffraction Investigation. *Solid State Ionics* **2011**, *193*, 1–4.
- (23) Kim, J. J.; Bishop, S. R.; Thompson, N.; Kuru, Y.; Tuller, H. L. Optically Derived Energy Band Gap States of Pr in Ceria. *Solid State Ionics* **2012**, *225*, 198–200.
- (24) Kim, J. J.; Bishop, S. R.; Thompson, N. J.; Chen, D.; Tuller, H. L. Investigation of Nonstoichiometry in Oxide Thin Films by Simultaneous in Situ Optical Absorption and Chemical Capacitance Measurements: Pr-Doped Ceria, a Case Study. *Chem. Mater.* **2014**, *26*, 1374–1379.
- (25) Chen, D.; Bishop, S. R.; Tuller, H. L. Non-Stoichiometry in Oxide Thin Films: A Chemical Capacitance Study of the Praseodymium-Cerium Oxide System. *Adv. Funct. Mater.* **2013**, *23*, 2168–2174.
- (26) Chen, D.; Bishop, S. R.; Tuller, H. L. Non-Stoichiometry in Oxide Thin Films Operating under Anodic Conditions: A Chemical Capacitance Study of the Praseodymium-Cerium Oxide System. *Chem. Mater.* **2014**, *26*, 6622–6627.
- (27) Chen, D.; Tuller, H. L. Voltage-Controlled Nonstoichiometry in Oxide Thin Films: $\text{Pr}_{0.1}\text{Ce}_{0.9}\text{O}_{2-\delta}$ Case Study. *Adv. Funct. Mater.* **2014**, *24*, 7638–7644.
- (28) Kim, J. J.; Bishop, S. R.; Chen, D.; Tuller, H. L. Defect Chemistry of Pr Doped Ceria Thin Films Investigated by in Situ Optical and Impedance Measurements. *Chem. Mater.* **2017**, *29*, 1999–2007.
- (29) Nicolle, C.; Kalaev, D.; Tuller, H. L. Mixed Conductivity and Oxygen Surface Exchange Kinetics of Lanthanum-Praseodymium Doped Cerium Dioxide. *Solid State Ionics* **2019**, *331*, 96–101.
- (30) Schröder, S.; Fritze, H.; Bishop, S.; Chen, D.; Tuller, H. L. Thin-Film Nano-Thermogravimetry Applied to Praseodymium-Cerium Oxide Films at High Temperatures. *Appl. Phys. Lett.* **2018**, *112*, 213502.
- (31) Kuru, Y.; Marrocchelli, D.; Bishop, S. R.; Chen, D.; Yildiz, B.; Tuller, H. L. Anomalous Chemical Expansion Behavior of $\text{Pr}_{0.2}\text{Ce}_{0.8}\text{O}_{2-\delta}$ Thin Films Grown by Pulsed Laser Deposition. *J. Electrochem. Soc.* **2012**, *159*, F799–F803.
- (32) Sheth, J.; Chen, D.; Kim, J. J.; Bowman, W. J.; Crozier, P. A.; Tuller, H. L.; Misture, S. T.; Zdziszynski, S.; Sheldon, B. W.; Bishop, S. R. Coupling of Strain, Stress, and Oxygen Non-Stoichiometry in Thin Film $\text{Pr}_{0.2}\text{Ce}_{0.8}\text{O}_{2-\delta}$. *Nanoscale* **2016**, *8*, 164990–16510.
- (33) Swallow, J. G.; Kim, J. J.; Kabir, M.; Smith, J. F.; Tuller, H. L.; Bishop, S. R.; Van Vliet, K. J. Operando Reduction of Elastic Modulus in $(\text{Pr}, \text{Ce})\text{O}_{2-\delta}$ Thin Films. *Acta Mater.* **2016**, *105*, 16–24.
- (34) Swallow, J. G.; Youssef, M.; Van Vliet, K. J. Defect-Mediated Mechanics in Non-Stoichiometric Oxide Films. *MRS Adv.* **2018**, *3*, 537–545.
- (35) Swallow, J. G.; Lee, J. K.; Defferriere, T.; Hughes, G. M.; Raja, S. N.; Tuller, H. L.; Warner, J. H.; Van Vliet, K. J. Atomic Resolution Imaging of Nanoscale Chemical Expansion in $\text{Pr}_x\text{Ce}_{1-x}\text{O}_{2-\delta}$ during In Situ Heating. *ACS Nano* **2018**, *12*, 1359–1372.

- (36) Lu, Q.; Vardar, G.; Jansen, M.; Bishop, S. R.; Waluyo, I.; Tuller, H. L.; Yildiz, B. Surface Defect Chemistry and Electronic Structure of $\text{Pr}_{0.1}\text{Ce}_{0.9}\text{O}_{2-\delta}$ Revealed in Operando. *Chem. Mater.* **2018**, *30*, 2600–2606.
- (37) Sheth, J.; Chen, D.; Tuller, H. L.; Misture, S. T.; Bishop, S. R.; Sheldon, B. W. Role of Grain Size on Redox Induced Compositional Stresses in Pr Doped Ceria Thin Films. *Phys. Chem. Chem. Phys.* **2017**, *19*, 12206–12220.
- (38) Bowman, W. J.; Zhu, J.; Sharma, R.; Crozier, P. A. Electrical Conductivity and Grain Boundary Composition of Gd-Doped and Gd/Pr Co-Doped Ceria. *Solid State Ionics* **2015**, *272*, 9–17.
- (39) Kok, D. J.; Irmscher, K.; Naumann, M.; Guguschev, C.; Galazka, Z.; Uecker, R. Temperature-Dependent Optical Absorption of SrTiO_3 . *Phys. Status Solidi A* **2015**, *212*, 1880–1887.
- (40) Wang, Z.; Mori, M.; Itoh, T. Thermal Expansion Properties of $\text{Sr}_{1-x}\text{La}_x\text{TiO}_3$ ($0 \leq x \leq 0.3$) Perovskites in Oxidizing and Reducing Atmospheres. *J. Electrochem. Soc.* **2010**, *157*, B1783.
- (41) Zhao, L.; Perry, N. H.; Daio, T.; Sasaki, K.; Bishop, S. R. Improving the Si Impurity Tolerance of $\text{Pr}_{0.1}\text{Ce}_{0.9}\text{O}_{2-\delta}$ SOFC Electrodes with Reactive Surface Additives. *Chem. Mater.* **2015**, *27*, 3065–3070.
- (42) Pergolesi, D.; Roddatis, V.; Fabbri, E.; Schneider, C. W.; Lippert, T.; Traversa, E.; Kilner, J. A. Probing the Bulk Ionic Conductivity by Thin Film Hetero-Epitaxial Engineering. *Sci. Technol. Adv. Mater.* **2015**, *16*, No. 015001.
- (43) Birkholz, M. *Thin Film Analysis by X-Ray Scattering*; Wiley: Weinheim, Germany, 2006.
- (44) Schweiger, S.; Kubicek, M.; Messerschmitt, F.; Murer, C.; Rupp, J. L. M. A Microdot Multilayer Oxide Device: Let Us Tune the Strain-Ionic Transport Interaction. *ACS Nano* **2014**, *8*, 5032–5048.
- (45) Weber, W. H.; Hass, K. C.; McBride, J. R. Raman Study of CeO_2 : Second-Order Scattering, Lattice dynamics, and Particle-Size Effects. *Phys. Rev. B* **1993**, *48*, 178–185.
- (46) Westermann, A.; Geantet, C.; Vernoux, P.; Lorient, S. Defects Band Enhanced by Resonance Raman Effect in Praseodymium Doped CeO_2 . *J. Raman Spectrosc.* **2016**, *47*, 1276–1279.
- (47) Kraynis, O.; Makagon, E.; Mishuk, E.; Hartstein, M.; Wachtel, E.; Lubomirsky, I.; Livneh, T. Suitability of Raman Spectroscopy for Assessing Anisotropic Strain in Thin Films of Doped Ceria. *Adv. Funct. Mater.* **2019**, *29*, 1804433.
- (48) Keeble, D. J.; Wicklein, S.; Jin, L.; Jia, C. L.; Egger, W.; Dittmann, R. Nonstoichiometry Accommodation in SrTiO_3 Thin Films Studied by Positron Annihilation and Electron Microscopy. *Phys. Rev. B* **2013**, *87*, 195409.
- (49) Ohnishi, T.; Shibuya, K.; Yamamoto, T.; Lippmaa, M. Defects and Transport in Complex Oxide Thin Films. *J. Appl. Phys.* **2008**, *103*, 103703.
- (50) Fluri, A.; Pergolesi, D.; Roddatis, V.; Wokaun, A.; Lippert, T. In Situ Stress Observation in Oxide Films and How Tensile Stress Influences Oxygen Ion Conduction. *Nat. Commun.* **2016**, *7*, 10692.
- (51) Schichtel, N.; Korte, C.; Hesse, D.; Zakharov, N.; Butz, B.; Gerthsen, D.; Janek, J. On the Influence of Strain on Ion Transport: Microstructure and Ionic Conductivity of Nanoscale $\text{YSZ}/\text{Sc}_2\text{O}_3$ Multilayers. *Phys. Chem. Chem. Phys.* **2010**, *12*, 14596–14608.
- (52) Cavallaro, A.; Burriel, M.; Roqueta, J.; Apostolidis, A.; Bernardi, A.; Tarancón, A.; Srinivasan, R.; Cook, S. N.; Fraser, H. L.; Kilner, J. A.; McComb, D. W.; Santiso, J. Electronic Nature of the Enhanced Conductivity in YSZ-STO Multilayers Deposited by PLD. *Solid State Ionics* **2010**, *181*, 592–601.
- (53) Jin-Phillipp, N. Y.; Sata, N.; Maier, J.; Scheu, C.; Hahn, K.; Kelsch, M.; Rühle, M. Structures of BaF_2 - CaF_2 Heterolayers and Their Influences on Ionic Conductivity. *J. Chem. Phys.* **2004**, *120*, 2375–2381.
- (54) Song, K.; Schmid, H.; Srot, V.; Gilardi, E.; Gregori, G.; Du, K.; Maier, J.; Van Aken, P. A. Cerium Reduction at the Interface between Ceria and Yttria-Stabilised Zirconia and Implications for Interfacial Oxygen Non-Stoichiometry. *APL Mater.* **2014**, *2*, No. 032104.
- (55) Pergolesi, D.; Gilardi, E.; Fabbri, E.; Roddatis, V.; Harrington, G. F.; Lippert, T.; Kilner, J. A.; Traversa, E. Interface Effects on the Ionic Conductivity of Doped Ceria-Yttria-Stabilized Zirconia Heterostructures. *ACS Appl. Mater. Interfaces* **2018**, *10*, 14160–14169.
- (56) Balaji Gopal, C.; García-Melchor, M.; Lee, S. C.; Shi, Y.; Shavorskiy, A.; Monti, M.; Guan, Z.; Sinclair, R.; Bluhm, H.; Vojvodic, A.; Chueh, W. C. Equilibrium Oxygen Storage Capacity of Ultrathin $\text{CeO}_{2-\delta}$ Depends Non-Monotonically on Large Biaxial Strain. *Nat. Commun.* **2017**, *8*, 15360.
- (57) Fortner, J. A.; Buck, E. C. The Chemistry of the Light Rare-Earth Elements as Determined by Electron Energy Loss Spectroscopy. *Appl. Phys. Lett.* **1996**, *68*, 3817–3819.
- (58) Bowman, W. J.; March, K.; Hernandez, C. A.; Crozier, P. A. Measuring Bandgap States in Individual Non-Stoichiometric Oxide Nanoparticles Using Monochromated STEM EELS: The Praseodymium-Ceria Case. *Ultramicroscopy* **2016**, *167*, 5–10.
- (59) Kim, S.; Maier, J. On the Conductivity Mechanism of Nanocrystalline Ceria. *J. Electrochem. Soc.* **2002**, *149*, J73.
- (60) Göbel, M. C.; Gregori, G.; Guo, X.; Maier, J. Boundary Effects on the Electrical Conductivity of Pure and Doped Cerium Oxide Thin Films. *Phys. Chem. Chem. Phys.* **2010**, *12*, 14351–14361.
- (61) Harrington, G. F.; Sasaki, K.; Tuller, H. L. Unpublished Work.
- (62) Navrotsky, A. Nanoscale Effects on Thermodynamics and Phase Equilibria in Oxide Systems. *ChemPhysChem* **2011**, *12*, 2207–2215.
- (63) De Souza, R. A.; Gunkel, F.; Hoffmann-Eifert, S.; Dittmann, R. Finite-Size versus Interface-Proximity Effects in Thin-Film epitaxial SrTiO_3 . *Phys. Rev. B* **2014**, *89*, 241401.
- (64) Herklotz, A.; Lee, D.; Guo, E.-J.; Meyer, T. L.; Petrie, J. R.; Lee, H. N. Strain Coupling of Oxygen non-stoichiometry in Perovskite Thin Films. *J. Phys.: Condens. Matter* **2017**, *29*, 493001.
- (65) Sun, L.; Marrocchelli, D.; Yildiz, B. Edge Dislocation Slows down Oxide Ion Diffusion in Doped CeO_2 by Segregation of Charged Defects. *Nat. Commun.* **2015**, *6*, 6294.